

Weak and strong-coupling dynamics of quantum emitters in the vicinity of metallic films: role of electron spill-out

Vasilios Karanikolas^{a,*}, Ioannis Thanopoulos^b, Joel D. Cox^{c,d}, Takashi Kuroda^e, Jun-ichi Inoue^e, N. Asger Mortensen^{c,d}, Emmanuel Paspalakis^b, and Christos Tserkezis^{c†}

^aInternational Center for Young Scientists (ICYS),

National Institute for Materials Science (NIMS) 1-1 Namiki, Tsukuba, Ibaraki 305-0044, Japan, ^bMaterials Science Department,

School of Natural Sciences, University of Patras,

Patras 265 04, Greece, ^cCenter for Nano Optics, University of Southern Denmark, Campusvej 55, DK-5230 Odense M,

Denmark, ^dDanish Institute for Advanced Study,

University of Southern Denmark, Campusvej 55, DK-5230 Odense M, Denmark,

^eNational Institute for Materials Science (NIMS) 1-1 Namiki, Tsukuba, Ibaraki 305-0044, Japan

(Dated: February 23, 2021)

The relaxation of a quantum emitter (QE) near metal-dielectric layered nanostructures is investigated, with focus on the influence of plasmonic quantum effects. The Green's tensor approach, combined with the Feibelman d -parameter formalism, is used to calculate the Purcell factor and the dynamics of a two-level QE in the presence of the nanostructure. Focusing on the case of Na, we identify electron spill-out as the dominant source of quantum effects in jellium-like metals. Our results reveal a clear splitting in the emission spectrum of the emitter, and non-Markovian relaxation dynamics, implying strong light-matter coupling between them, a coupling that is not prevented by the quantum-informed optical response of the metal.

Introduction — Confining light in sub-diffraction volumes via surface plasmon polaritons (SPPs) has become common practice to enhance light-matter interactions in the past decade [1]. In information-processing applications, plasmonic nanostructures are combined with multi-level quantum emitters (QEs) which, depending on the desired functionality, can be natural (atoms, molecules) or artificial (quantum wells and dots, defects in diamonds, collective states in transition metal dichalcogenides or hexagonal boron nitride) [2–7]. By analogy to cavity QED [8, 9], metallic nanostructures play in such cases the role of the cavity [10–13]. Advanced fabrication techniques now enable the engineering of metal cavities with characteristic dimensions below 10 nm, and the precise positioning of QEs within them, to produce promising templates for bright single-photon emitters [14–18]. The plasmonic cavity is typically formed by a metallic substrate interacting with another metallic film or with dropcasted nanoparticles; separating the two plasmonic components by a thin dielectric spacer containing QEs in the form of defects, molecules, or quantum dots [19–22], the resulting intense electromagnetic (EM) fields, confined within minimized volumes, trigger extreme light-matter interactions.

Traditionally, in the local-response approximation (LRA) [23], the optical response of metals is described through the Drude model, or through experimentally measured bulk permittivities. But, as plasmonic cavities become narrower, the interaction strengths with the therein confined QEs are overestimated by LRA, as compared to experimental results [24–26], calling for amendment of the theoretical models [27–31]; the main missing element is information about quantum effects in the

metal. As a first extension of LRA, the hydrodynamic Drude model (HDM), which describes the motion of the compressible free-electron gas as a convective fluid, has met with considerable success [32–35], yet effects associated with electron spill-out still require a self-consistent treatment [36–38]. However, the ultimate goal of an *ab initio* optical response calculation for structures with sizes of 100 nm order at room temperature is out of computational reach [39]. A more efficient approach is based on the work of Feibelman [40], who bridged EM and *ab initio* calculations through appropriate surface-response functions, the d parameters, which need be calculated only once for a given surface, and can be implemented in a quantum-informed surface-response formalism (SRF) [31, 41–43]. The full QED problem is then described by quantum-corrected mesoscopic boundary conditions at the metal surface [31, 41]. Macroscopic QED [44, 45] allows to directly apply the rigorous Green's function approach developed within LRA, now corrected by SRF, without invoking quantum effects in a quasi-normal mode formalism [46–48].

To date, focus has been cast on the interaction of QEs with plasmonic nanostructures described by non-local dielectric functions (e.g. within HDM), identifying significant differences in both weak [49, 50] and strong-coupling regimes [51, 52], as compared to LRA. Here, we go one step further to explore, for the first time, the role of quantum-informed plasmonics in the population dynamics of the QE excited state under strong-coupling conditions, where QE and environment coherently exchange energy (observable through Rabi oscillations in the population and Rabi energy splittings in the emission spectra). We focus on insulator/metal (IM), insu-

lator/metal/insulator (IMI), and metal/insulator/metal (MIM) geometries [33, 53], for which the strong-coupling regime proves reachable even when quantum corrections in the metal are taken into account.

Theory — The QE is approximated as a two-level system with ground state $|g\rangle$ and excited state $|e\rangle$, transition frequency ω_0 , and dipole moment $\boldsymbol{\mu}$. Initially, the QE is in the excited state, and the EM field is in its vacuum state $|i\rangle = |e\rangle \otimes |0\rangle$, while the final state is $|f\rangle = |g\rangle \otimes \hat{f}_i^\dagger(\mathbf{r}, \omega)|0\rangle$, where the QE relaxes to the ground state by emitting a photon or exciting SPPs dressed states supported by the metallic nanostructures [54], and \hat{f}_i^\dagger denotes the bosonic creation operator of the dressed state i . The QE relaxation rate Γ is given by $\Gamma(\mathbf{r}, \omega) = \Gamma_0 \tilde{\Gamma}(\mathbf{r}, \omega)$, where $\Gamma_0 = \omega^3 \mu^2 / 3\pi c^3 \hbar \epsilon_0$ is the vacuum rate and $\tilde{\Gamma}(\mathbf{r}, \omega)$ is the Purcell factor of a QE placed at $\mathbf{r} = (0, 0, z)$ above a metal/dielectric interface; for a transition dipole moment perpendicular to the interface, the Purcell factor has the form

$$\tilde{\Gamma}_z(\mathbf{r}, \omega) = \sqrt{\epsilon_d} - \frac{3c}{2\omega} \text{Re} \left\{ \int_0^\infty dk_s \frac{k_s^3 R_{\text{TM}}}{k_{d,z} k_d^2} e^{2ik_{d,z}z} \right\}, \quad (1)$$

where R_{TM} is the generalized transverse magnetic (TM) Fresnel coefficient [55, 56].

Our material of choice is Na, whose work function is lower than that of the common plasmonic metals, Au and Ag, so as to focus on the electron spill-out effects [57, 58]. For the single dielectric/metal interface, the TM reflection coefficients take the form (assuming $d_{\parallel} = 0$, valid for Na) [43]

$$R_{\text{TM}} = \frac{\epsilon_m k_{d,z} - \epsilon_d k_{m,z} + i(\epsilon_m - \epsilon_d) k_s^2 d_{\perp}(\omega)}{\epsilon_m k_{d,z} + \epsilon_d k_{m,z} - i(\epsilon_m - \epsilon_d) k_s^2 d_{\perp}(\omega)}, \quad (2)$$

where ϵ_d and ϵ_m denote the permittivity of the dielectric (d) and metal (m), respectively, $k_0 = \omega/c$ is the free-space wave vector, $k_j = \sqrt{\epsilon_j} k_0$ (with $j=m,d$) is the wave vector of each medium, analyzed in in-plane (k_s) and normal ($k_{j,z} = \sqrt{k_j^2 - k_s^2}$) components. For Na we use a Drude model $\epsilon(\omega) = 1 - \omega_p^2 / (\omega^2 + i\omega\gamma)$, with ω_p being the plasma frequency and γ the damping rate, taken as $\hbar\omega_p = 5.9$ eV and $\hbar\gamma = 0.1$ eV, while d_{\perp} is given by Lorentzian-fitted data extracted from *ab initio* calculations for jellium [42, 43].

The relaxation of the quantum emitter is described by its emission spectrum [59, 60]

$$S(\omega, \mathbf{r}) = \left| \frac{(\mu^2 \omega^2 / \sqrt{2\pi\epsilon_0 c^2}) \hat{\mathbf{n}} \cdot \mathbf{G}(\omega, \mathbf{r}, \mathbf{r}_d)}{\omega_0 - \omega - \int_0^\infty d\omega' J(\omega_0, \omega', \mathbf{r}) / (\omega' - \omega)} \right|^2 \quad (3)$$

in the frequency domain, and by the time-dependent QE excited state probability amplitude, $c_1(t)$, given by the solution of the integro-differential equation [62–65]

$$\frac{dc_1(t)}{dt} = i \int_0^t dt' K(t-t') c_1(t'). \quad (4)$$

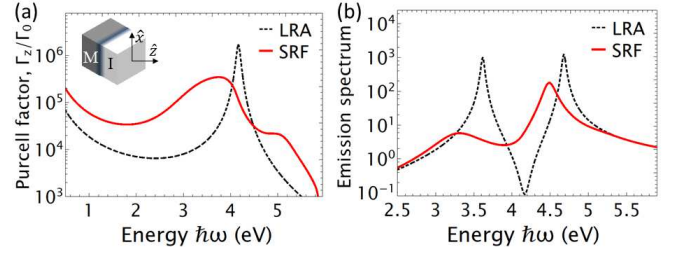


Figure 1. A QE with z -oriented transition dipole moment, placed 1 nm away from an air/Na IM interface. (a) Purcell factor and (b) emission spectrum within LRA (black dashed lines) and SRF (red solid lines).

The kernel of Eq. (4) is given by $K(\tau) = ie^{i\omega_0\tau} \int_0^\infty J(\omega_0, \omega, \mathbf{r}) e^{-i\omega\tau} d\omega$, where $J(\omega_0, \omega, \mathbf{r}) = \tilde{\Gamma}_i(\omega, \mathbf{r}) / [2\pi\tau_0]$ is the spectral density, ω_0 is the energy difference between the ground and excited QE states, and $\tau_0 = 1/\Gamma_0(\omega_0)$ is its free-space lifetime [62–65]. In Eq. (3), \mathbf{r}_d is the position where the signal is detected, and \mathbf{r} is the position of the QE, while ω is the emission frequency of the combined QE/Na system [59, 60]. Eq. (3) implies that if the QE–nanostructure coupling strength is high enough, the emission spectrum will feature a doublet of emission peaks, whose energy difference defines the Rabi splitting $\hbar\Omega$. More details for the macroscopic QED model used can be found on [61].

Results — We begin our investigation of the influence of spill-out on the emission properties of QEs by revisiting the simple IM case. In Fig. 1(a) we present the Purcell factor as a function of the QE transition energy for a QE placed 1 nm away from an air–Na IM interface, as evaluated by LRA and SRF. We directly observe that the highest Purcell factor value within SRF has a redshifted peak value that is one order of magnitude smaller than the corresponding LRA result, and the SPP-originated resonance around $\hbar\omega = \hbar\omega_p/\sqrt{2} = 4.125$ eV is broader. These features are related to additional material losses due to surface-enabled Landau damping [66]. Nevertheless, at lower frequencies, away from the SPP resonance, the SRF Purcell factor is in fact higher than the one predicted by LRA. Similar results have been discussed in Ref. 43, thus validating the Green’s tensor formalism employed here.

The emission spectrum of a QE with transition energy $\hbar\omega_0 = 4.125$ eV and free-space lifetime $\tau_0 = 0.1$ ns is presented in Fig. 1(b), where the Purcell factors of Fig. 1(a) are used. In the LRA description, the emission spectrum features two sharp peaks, splitting by $\hbar\Omega = 1.06$ eV around the QE transition energy. When the quantum aspects of the response of the metal are introduced through SRF, the two emission peaks become broader due to the higher material losses, but the Rabi splitting increases to $\hbar\Omega = 1.3$ eV; the latter phenomenon stems from the dependence of the QE emission on the *entire spectrum* of

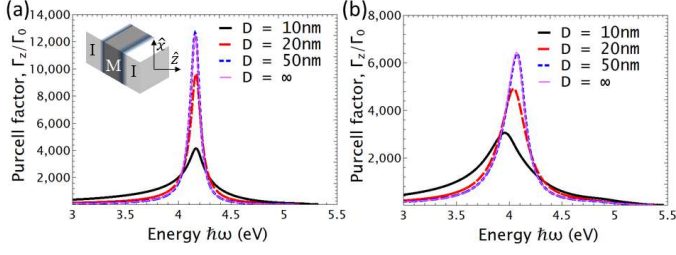


Figure 2. Purcell factor within (a) LRA and (b) SRF of a QE placed 5 nm away from an IMI nanostructure, for different metal thicknesses $D = 10$ (black solid line), 20 (red dotted line) and 50 nm (blue dashed line). The thin purple shows the corresponding IM result.

the Purcell factor, which is higher within SRF away from the SPP resonance [Fig. 1(a)] [42].

Turning to the IMI case, where air is considered as the insulating medium, we examine the corresponding Purcell factor in Figs. 2(a) and (b) within LRA and SRF, respectively, for metal layer thicknesses $D = 10$, 20, and 50 nm. Specifically, we set the distance between the QE and the insulator/metal interface to $z_{\text{QE}} = 5$ nm, noting that the Purcell factors calculated for the IM and the IMI geometry exhibit negligible differences for smaller values $z_{\text{QE}} \lesssim 2$ nm. In the case of LRA, the Purcell factor has its highest value at the SPP energy for all layer thicknesses. On the other hand, when SRF is taken into account, the maximum Purcell factor is roughly halved, and its peak positions redshift significantly as the metal thickness decreases. For the thinnest layer ($D = 10$ nm), the resonance within SRF has shifted by more than $\hbar\omega = 0.2$ eV compared to LRA. For increasing metal thickness (above $D = 50$ nm), the Purcell factor for the IMI case converges to the IM result.

While the IMI architecture is instructive, we will focus on the MIM structure, which is expected to display all the advantages of plasmonic cavities discussed in the introduction. In Figs. 3(a,b) we compare LRA and SRF contour plots of the Purcell factor as a function of the QE emission energy and the thickness D of the insulator layer (assumed air here) for a QE placed in the middle of the insulator layer of the MIM structure ($z_{\text{QE}} = 0$). In both plots we observe that, for small D , the Purcell factor is significantly enhanced compared to the reference free-space value. In LRA, the peak of the Purcell factor coincides with the SPP resonance, while for higher energies there is a sharp drop of its value, connected with the absence of plasmon polariton modes in the band-gap region of the MIM structure [67]. On the other hand, SRF reproduces the expected redshift of the Purcell factor spectrum, while considerable enhancement is observed inside the band-gap, as a result of the quantum effects captured by the Feibelman parameters. As the thickness of the insulator increases, surface effects become less im-

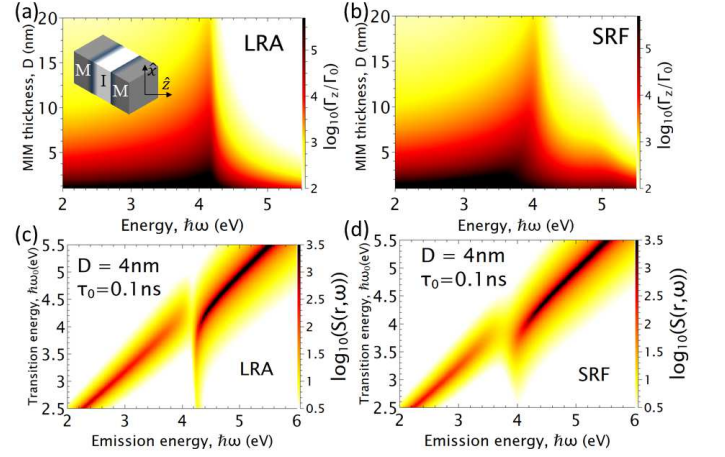


Figure 3. Contour plot of the Purcell factor of a QE, as a function of emission energy and dielectric layer thickness D , calculated within (a) LRA and (b) SRF, and the corresponding contours of the emission spectra as a function of the QE emission and transition energies obtained with (c) LRA and (d) SRF. The QE, with $\tau_0 = 0.1$ ns, is placed in the middle of the insulator layer of an MIM structure with dielectric-layer thickness $D = 4$ nm.

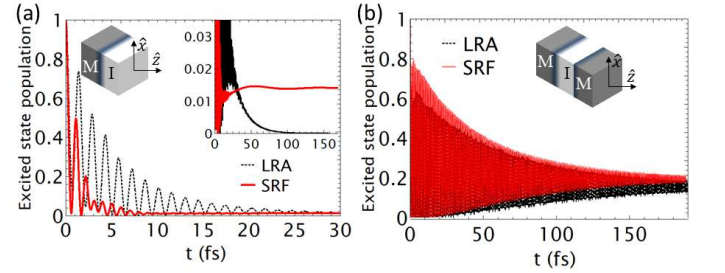


Figure 4. Population of the excited state of a two-level QE with $\hbar\omega_0 = 3$ eV and $\tau_0 = 0.1$ ns, as a function of time t . (a) The QE is placed 1 nm away from an IM geometry. (b) The QE is placed in the middle of a MIM geometry with dielectric-layer thickness $D = 2$ nm. In both panels, black and red lines correspond to results within LRA and SRF, respectively.

portant and the spectra obtained within the two models converge. What is evident from the large Purcell-factor enhancements of Figs. 3(a,b) is that the QE–MIM interaction can enter the strong coupling regime, as verified by the emission-spectrum contour plots of Fig. 3(c,d), where clear anticrossings can be observed not only within LRA, but also in the SRF case. Naturally, the emission double-peak features are sharper in the LRA description, and are broadened when additional loss channels due to surface effects are considered, but the observed Rabi splitting clearly survives.

The QE excited state population dynamics presented in Fig. 4 exhibits strong oscillations, with very different features from simple exponential relaxation within the Markovian (weak coupling) approximation, where memory effects in Eq. (4) are ignored. For a QE with tran-

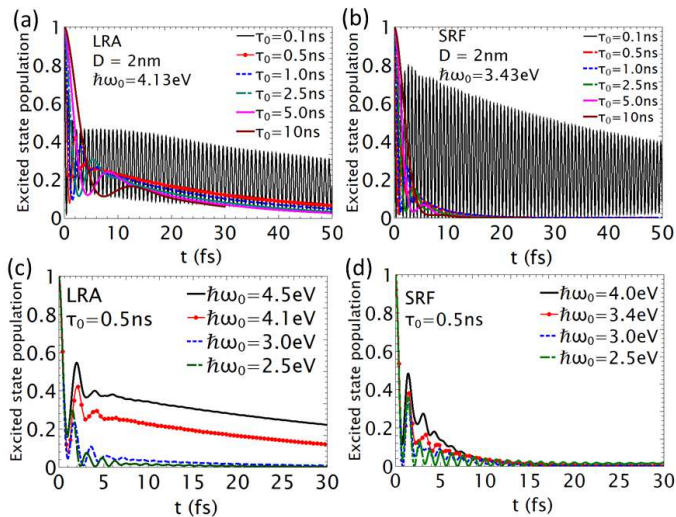


Figure 5. Population of the excited state of a two-level QE as a function of time, within LRA (a,c) and SRF (b,d). The QE is placed in the middle of a MIM geometry of thickness $D = 2$ nm. (a,b) The values of τ_0 considered are displayed in the insets. The transition energy of the QE is $\hbar\omega_0 = 4.13$ eV (LRA) and $\hbar\omega_0 = 3.43$ eV (SRF). (c,d) The values of $\hbar\omega_0$ considered are shown in the insets, for a QE with $\tau_0 = 0.5$ ns.

sition energy $\hbar\omega_0 = 3$ eV and vacuum relaxation rate $\tau_0 = 0.1$ ns, Fig. 4(a) shows the excited state dynamics when $z_{\text{QE}} = 1$ nm in the IM geometry. In the LRA description, we observe that after a few rapid oscillations, the QE relaxes to the ground state within a time-span of 30 fs. Faster relaxation to the ground state is predicted in SRF, although a closer look in the inset of Fig. 4(a) reveals that in this case the excited state remains partially populated, $|c_{\text{nL}}|^2 = 0.01$, even at longer times.

To directly compare IM and MIM geometries, we consider a QE centered in an insulating (air) layer of $D = 2$ nm thickness sandwiched between metal regions, i.e., maintaining a 1 nm distance from the metal/dielectric interfaces. Here, the QE excited state population dynamics presented in Fig. 4(b) is characterized by strong oscillatory behavior, with large population values persisting over long time spans. While the QE eventually fully relaxes, at later times, to the ground state in LRA, the SRF calculations accounting for the quantum response predicts that about $\sim 20\%$ of its initial population remains trapped in the excited state.

In Fig. 5 we present the excited state population dynamics of a QE placed in the middle of a MIM cavity having an insulator (air) layer thickness of $D = 2$ nm when different free-space relaxation rates τ_0 are considered. Choosing the associated QE transition energy matching the highest value shown in the Purcell factor spectra of Fig. 3, LRA and SRF models are contrasted in Figs. 5(a,b) for $\hbar\omega_0 = 4.13$ eV and $\hbar\omega_0 = 3.43$ eV, respectively. In both panels we observe strong and rapid

Rabi oscillations; as the value of the free-space lifetime decreases from $\tau_0 = 10$ to 0.1 ns, the QE/MIM coupling increases, the oscillation period decreases, and non-Markovian effects become stronger, as anticipated. We also observe that the population oscillations are denser in the SRF case.

Finally, we explore the influence of the QE transition energy, $\hbar\omega_0$, on the excited state population dynamics in Figs. 5(c,d), taking a QE free-space lifetime of $\tau_0 = 0.5$ ns. Different values of the QE transition energy are considered, including those matching the SPP energies indicated in the Purcell factor spectrum of Fig. 3. Fig. 5(c) shows the LRA calculation, where we observe that, after a few oscillations, the population dynamics remains partially trapped—although, eventually, it fully relaxes at later times. As the QE transition energy decreases, moving out of resonance with the SPP at its associated Purcell enhancement, the partially transient trapped population steadily decreases. In the SRF case, we also observe a highly oscillatory behavior of the excited state population density, a sign that the non-Markovian signature is retained. Although the partially excited population trapping is smaller, strong oscillations are still present, with reduced period, a sign that the overall QE–MIM interaction is higher when the quantum aspects of the metal response are taken into account.

Summary — We theoretically explored the emission properties of a QE placed in proximity to IM, IMI, and MIM geometries in the weak and strong coupling regimes. Focusing on Na as a plasmonic metal dominated by electron spill-out, we described its quantum-informed optical response through SRF, in which the Feibelman d parameters for the centroid of induced charge incorporate first-principles calculations. Although quantum effects introduce additional losses in the metal, the QE/MIM cavity system is found to operate in the strong-coupling regime, manifested as a Rabi splitting in the emission spectrum, and through Rabi oscillations in the relaxation dynamics of the QE excited state, with a highly non-Markovian character. SRF bridges, therefore, *ab initio* approaches with classical EM calculations in a simple and elegant way, suitable for quantum-optical studies at the nanoscale.

Acknowledgments — J. D. C. is a Sapere Aude research leader supported by Independent Research Fund Denmark (grant no. 0165-00051B). N. A. M. is a VILLUM Investigator supported by VILLUM FONDEN (grant no. 16498). E.P.’s work is co-financed by Greece and the European Union (project code name POLISIMULATOR).

* KARANIKOLAS.Vasileios@nims.go.jp

† ct@mci.sdu.dk

[1] E. Ozbay, Science **311**, 189 (2006).

- [2] A. V. Akimov, A. Mukherjee, C. L. Yu, D. E. Chang, A. S. Zibrov, P. R. Hemmer, H. Park, and M. D. Lukin, *Nature* **450**, 402 (2007).
- [3] D. E. Chang, A. S. Sørensen, E. A. Demler, and M. D. Lukin, *Nature Physics* **3**, 807 (2007).
- [4] A. Goban, C.-L. Hung, S.-P. Yu, J. Hood, J. Muniz, J. Lee, M. Martin, A. McClung, K. Choi, D. Chang, O. Painter, and H. Kimble, *Nature Communications* **5**, 3808 (2014).
- [5] J. D. Hood, A. Goban, A. Asenjo-Garcia, M. Lu, S.-P. Yu, D. E. Chang, and H. J. Kimble, *Proceedings of the National Academy of Sciences* **113**, 10507 (2016).
- [6] A. I. Fernández-Domínguez, S. I. Bozhevolnyi, and N. A. Mortensen, *ACS Photonics* **5**, 3447 (2018).
- [7] M. Koperski, D. Vaclavkova, K. Watanabe, T. Taniguchi, K. S. Novoselov, and M. Potemski, *Proceedings of the National Academy of Sciences* **117**, 13214 (2020).
- [8] L. Mandel and E. Wolf, *Optical Coherence and Quantum Optics* (Cambridge University Press, 1995).
- [9] M. O. Scully and M. S. Zubairy, *Quantum Optics* (Cambridge University Press, 1997).
- [10] P. Törmä and W. L. Barnes, *Reports on Progress in Physics* **78**, 013901 (2015).
- [11] M. Pelton, *Nature Photonics* **9**, 427 (2015).
- [12] S. I. Bozhevolnyi and J. B. Khurgin, *Nature Photonics* **11**, 398 (2017).
- [13] J. J. Baumberg, J. Aizpurua, M. H. Mikkelsen, and D. R. Smith, *Nature Materials* **18**, 668-678 (2019).
- [14] C. Manolatou and F. Rana, *IEEE Journal of Quantum Electronics* **44**, 435 (2008).
- [15] G. M. Akselrod, C. Argyropoulos, T. B. Hoang, C. Ciraci, C. Fang, J. Huang, D. R. Smith, and M. H. Mikkelsen, *Nature Photonics* **8**, 835 (2014).
- [16] A. Rose, T. B. Hoang, F. McGuire, J. J. Mock, C. Ciraci, D. R. Smith, and M. H. Mikkelsen, *Nano Letters* **14**, 4797 (2014).
- [17] R. Chikkaraddy, B. de Nijs, F. Benz, S. J. Barrow, O. A. Scherman, E. Rosta, A. Demetriadou, P. Fox, O. Hess, and J. J. Baumberg, *Nature* **535**, 127 (2016).
- [18] M. A. May, D. Fialkow, T. Wu, K.-D. Park, H. Leng, J. A. Kropp, T. Gougousi, P. Lalanne, M. Pelton, and M. B. Raschke, *Advanced Quad. Tech.* **3**, 1900087 (2020).
- [19] S. I. Bogdanov, M. Y. Shalaginov, A. S. Lagutchev, C.-C. Chiang, D. Shah, A. S. Baburin, I. A. Ryzhikov, I. A. Rodionov, A. V. Kildishev, A. Boltasseva, and V. M. Shalaev, *Nano Letters* **18**, 4837 (2018).
- [20] J. M. Katzen, C. Tserkezis, Q. Cai, L. H. Li, J. M. Kim, G. Lee, G.-R. Yi, W. R. Hendren, E. J. G. Santos, R. M. Bowman, and F. Huang, *ACS Applied Materials & Interfaces* **12**, 19866 (2020).
- [21] O. S. Ojambati, W. M. Deacon, R. Chikkaraddy, C. Readman, Q. Lin, Z. Koczor-Benda, E. Rosta, O. A. Scherman, and J. J. Baumberg, *ACS Photonics* **7**, 2337 (2020).
- [22] F. Ding, Y. Yang, R. A. Deshpande, and S. I. Bozhevolnyi, *Nanophotonics* **7**, 1129 (2018).
- [23] U. Hohenester, *Nano and Quantum Optics: An Introduction to Basic Principles and Theory* (Springer, 2020).
- [24] C. Ciraci, R. T. Hill, J. J. Mock, Y. Urzhumov, A. I. Fernández-Domínguez, S. A. Maier, J. B. Pendry, A. Chilkoti, and D. R. Smith, *Science* **337**, 1072 (2012).
- [25] K. J. Savage, M. M. Hawkeye, R. Esteban, A. G. Borisov, J. Aizpurua, and J. J. Baumberg, *Nature* **491**, 574 (2012).
- [26] J. A. Scholl, A. L. Koh, and J. A. Dionne, *Nature* **483**, 421 (2012).
- [27] I. Romero, J. Aizpurua, G. W. Bryant, F. J. García de Abajo, *Optics Express* **14**, 9988 (2006).
- [28] R. Esteban, A. G. Borisov, P. Nordlander and J. Aizpurua, *Nature Communications* **3**, 825 (2012).
- [29] Y. Luo, A. I. Fernández-Domínguez, A. Wiener, S. A. Maier and J. B. Pendry, *Physical Review Letters* **111**, 093901 (2013).
- [30] S. Raza, N. Stenger, S. Kadkhodazadeh, S. V. Fischer, N. Kostesha, A.-P. Jauho, A. Burrows, M. Wubs, and N. A. Mortensen, *Nanophotonics* **2**, 131 (2013).
- [31] Y. Yang, D. Zhu, W. Yan, A. Agarwal, M. Zheng, J. D. Joannopoulos, P. Lalanne, T. Christensen, K. K. Berggren, and M. Soljačić, *Nature* **576**, 248 (2019).
- [32] A. Moreau, C. Ciraci, and D. R. Smith, *Physical Review B* **87**, 045401 (2013).
- [33] S. Raza, T. Christensen, M. Wubs, S. I. Bozhevolnyi, and N. A. Mortensen, *Physical Review B* **88**, 115401 (2013).
- [34] N. A. Mortensen, S. Raza, M. Wubs, T. Søndergaard, and S. I. Bozhevolnyi, *Nature Communications* **5**, 3809 (2014).
- [35] C. Tserkezis, A. T. M. Yeşilyurt, J.-S. Huang, and N. A. Mortensen, *ACS Photonics* **5**, 5017 (2018).
- [36] G. Toscano, J. Straubel, A. Kwiatkowski, C. Rockstuhl, F. Evers, H. Xu, N. A. Mortensen and M. Wubs, *Nature Communications* **6**, 7132 (2015).
- [37] W. Yan, *Physical Review B* **91**, 115416 (2015).
- [38] C. Ciraci and F. Della Sala, *Physical Review B* **93**, 205405 (2016).
- [39] A. Varas, P. García-González, J. Feist, F. García-Vidal, and A. Rubio, *Nanophotonics* **5**, 409 (2016).
- [40] P. Feibelman, *Progress in Surface Science* **12**, 287 (1982).
- [41] W. Yan, M. Wubs, and N. Asger Mortensen, *Physical Review Letters* **115**, 137403 (2015).
- [42] T. Christensen, W. Yan, A.-P. Jauho, M. Soljačić, and N. A. Mortensen, *Physical Review Letters* **118**, 157402 (2017).
- [43] P. A. D. Gonçalves, T. Christensen, N. Rivera, A.-P. Jauho, N. A. Mortensen, and M. Soljačić, *Nature Communications* **11**, 366 (2020).
- [44] N. Rivera and I. Kaminer, *Nature Reviews Physics* **2**, 538 (2020).
- [45] K. Head-Marsden, J. Flick, C. J. Ciccarino, and P. Narang, *Chemical Reviews* **121** (2021), 10.1021/acs.chemrev.0c00620.
- [46] P. Lalanne, W. Yan, K. Vynck, C. Sauvan, and J.-P. Hugonin, *Laser & Photonics Reviews* **12**, 1700113 (2018).
- [47] M. K. Dezfouli, C. Tserkezis, N. A. Mortensen, and S. Hughes, *Optica* **4**, 1503 (2017).
- [48] S. Franke, S. Hughes, M. K. Dezfouli, P. T. Kristensen, K. Busch, A. Knorr, and M. Richter, *Physical Review Letters* **122**, 213901 (2019).
- [49] C. Tserkezis, N. Stefanou, M. Wubs, and N. A. Mortensen, *Nanoscale* **8**, 17532 (2016).
- [50] T. Christensen, W. Yan, S. Raza, A.-P. Jauho, N. A. Mortensen, and M. Wubs, *ACS Nano* **8**, 1745 (2014).
- [51] C. Tserkezis, M. Wubs, and N. A. Mortensen, *ACS Photonics* **5**, 133 (2018).
- [52] C. Tserkezis, A. I. Fernández-Domínguez, P. A. D. Gonçalves, F. Todisco, J. D. Cox, K. Busch, N. Stenger, S. I. Bozhevolnyi, N. A. Mortensen, and C. Wolff, *Reports on Progress in Physics* **83**, 082401 (2020).
- [53] C. L. C. Smith, N. Stenger, A. Kristensen, N. A.

- Mortensen, and S. I. Bozhevolnyi, *Nanoscale* **7**, 9355 (2015).
- [54] H. T. Dung, L. Knöll, and D.-G. Welsch, *Physical Review A* **65**, 043813 (2002).
- [55] C. T. Tai, *Dyadic Green Functions in Electromagnetic Theory* (Oxford University Press, Oxford, 1994).
- [56] S. Scheel and S. Y. Buhmann, *Acta Physical Slovaca* **58** 675 (2009).
- [57] F. J. García de Abajo, *Journal of Physical Chemistry C* **112**, 17983 (2008).
- [58] A. R. Echarri, P. A. D. Gonçalves, C. Tserkezis, F. J. García de Abajo, N. A. Mortensen, and J. D. Cox, arXiv:2009.10821.
- [59] C. Van Vlack, P. T. Kristensen, and S. Hughes, *Physical Review B* **85**, 075303 (2012).
- [60] V. Karanikolas, I. Thanopoulos, and E. Paspalakis, *Physical Review Research* **2**, 033141 (2020).
- [61] See Supplemental Material for details on the calculation of the Green's tensor for the IM, IMI and MIM geometries including the SRF boundary conditions. The macroscopic QED theory is used to extract Eqs. (3) and (4).
- [62] A. Gonzalez-Tudela, P. A. Huidobro, L. Martín-Moreno, C. Tejedor, and F. J. García-Vidal, *Physical Review B* **89**, 041402(R) (2014).
- [63] R.-Q. Li, D. Hernáñez-Peréz, F. J. García-Vidal, and A. I. Fernández-Domínguez, *Physical Review Letters* **117**, 107401 (2016).
- [64] I. Thanopoulos, V. Yannopoulos, and E. Paspalakis, *Physical Review B* **95**, 075412 (2017).
- [65] I. Thanopoulos, V. Karanikolas, N. Iliopoulos, and E. Paspalakis, *Physical Review B* **99**, 195412 (2019).
- [66] C. Tserkezis, N. A. Mortensen, and M. Wubs, *Physical Review B* **96**, 085413 (2017).
- [67] C. A. Marocico and J. Knoester, *Physical Review A* **84**, 053824 (2011).